Ground state of the holes localized in II-VI quantum dots with Gaussian potential profiles

M. A. Semina, A. A. Golovatenko, and A. V. Rodina
Ioffe Institute, 194021, St. Petersburg, Russia

(Received 3 August 2015; revised manuscript received 21 December 2015; published 12 January 2016)

We report on a theoretical study of the hole states in II-IV quantum dots of spherical and ellipsoidal shapes, described by smooth potential confinement profiles that can be modeled by Gaussian functions in all three dimensions. The universal dependencies of the hole energy, g factor, and localization length on the quantum dot barrier height, as well as the ratio of effective masses of the light and heavy holes are presented for the spherical quantum dots. The splitting of the fourfold degenerate ground state into two doublets is derived for anisotropic (oblate or prolate) quantum dots. Variational calculations are combined with numerical ones in the framework of the Luttinger Hamiltonian. Constructed trial functions are optimized by comparison with the numerical results. The effective hole g factor is found to be independent of the quantum dot size and barrier height and is approximated by a simple universal expression depending only on the effective mass parameters. The results can be used for interpreting and analyzing experimental spectra measured in various structures with quantum dots of different semiconductor materials.

DOI: 10.1103/PhysRevB.93.045409

I. INTRODUCTION

Quantum dots (QDs), sometimes referred to as nanocrystals (NCs) in literature, are systems with good prospects for nanotechnology. Physically, the QDs are tiny semiconductor nanoparticles, which are formed in various dielectric or semiconductor matrices by different methods. Among them, the basic ones are the chemical synthesis and epitaxy used to fabricate, respectively, the colloidal and epitaxial QDs. Depending on the used semiconductors and the fabrication methods, QDs can have various shapes and sizes. Carrier localization in QDs makes the interaction between charge carriers more efficient as compared with bulk materials, and many effects that are weak in bulk materials become observable. Thus the development of new methods for the calculation of the wave functions and energy spectra of charge carriers is very important for designing QD structures.

The incentive to our study was the renewed interest in II-VI QDs for various applications. In particular, the epitaxial CdSe/Zn(S,Se) QDs have been successfully used as an active region in laser heterostructures pumped optically or by an electron beam [1,2]. Besides, they have been recognized as promising candidates for room-temperature single-photon emission and production of photon pairs due to strong carrier confinement and distinct biexciton performance [3–5]. The self-formation of these nanostructures takes place when a CdSe insertion of a fraction monolayer (ML) thickness is deposited within a Zn(S,Se) matrix. Previously, this insertion was considered as a disordered quantum well, where nanoislands with high Cd content, x, are formed within the matrix with lower x [6,7]. Thorough transmission electron microscopy (TEM) studies [8], however, have shown that the Cd content in the Cd-rich nanoislands can be as high as 80% in the center, decreasing towards the periphery, while the Cd concentration in the surrounding area approaches 20% only. The average lateral sizes of the nanoislands are about 5 nm, while the sizes in the growth direction are somewhat smaller. These findings make it possible to consider the nanoislands as oblate ellipsoidal QDs. Such an asymmetric shape influences the energy splitting of both exciton and biexciton states in the single CdSe/ZnSe QD [9], which is important for the generation of entangled photon pairs. The CdSe/Zn(S,Se) structures exhibited long-lived electron spin coherence, related likely to the three-dimensional localization potential [10]. Recently, it has been demonstrated that at a certain deposited amount of CdSe the nanoislands can be quite isolated [11]. Importantly, the change of the concentration between the dot and barrier regions in the epitaxial CdSe/Zn(S,Se) QDs is not abrupt but gradual due to diffusion and segregation processes.

The II-VI QDs with such a gradual composition variation are expected to demonstrate an improved radiative emission. Indeed, for a long time, the biexciton performance of the chemically synthesized colloidal QDs was suffering from a high rate of nonradiative Auger recombination. To overcome this problem, colloidal CdSe-based nanocrystal heterostructures with gradually changing composition were synthesized and reported in Ref. [12]. The nonradiative Auger processes are suppressed in such structures due to smoothing of the confining potential [13–16]. Further progress in the analysis of optical phenomena in the II-VI QDs and the manufacturing of efficient nanoemitters of quantum light requires an elaborated model description of quantum states in the ellipsoidal QDs with a smooth potential profile. Among a variety of theoretical methods, including atomistic tight-binding [17,18] or pseudopotential calculations [19], and $\boldsymbol{kp}$ theory, the latter provides a reasonable compromise between accuracy and computational complexity. The $\boldsymbol{kp}$ method is particularly suitable for nanostructures with a smooth potential profile, where interface effects play a minor role.

In the most simple effective mass model of a nondegenerate parabolic band, various kinds of confinement potentials for QDs were theoretically studied: an abrupt potential with infinite and finite barriers [20–25], a parabolic potential [26,27], and various kinds of smooth potentials with finite height [28–31]. The parabolic potential was also shown to be a good approximation for the in-plane smooth profile of the lens-shaped self-assembled QDs [32]. However, to describe properly the energy spectra of the holes confined in QDs, one has to take into account the complex structure of the valence band. In widely used semiconductors (including II-VI),

the top of the valence band is fourfold degenerate and has Γ_8 symmetry and can be described by the Luttinger Hamiltonian [33]. The fine energy structure of the hole states defines the selection rules for interband transitions. Moreover, the Zeeman splitting in the external magnetic field is determined by the light- and heavy-hole splitting and mixing [25,34,35]. Therefore understanding the characteristic properties of the hole states in QDs is important for designing structures with the required optical properties.

For the spherical NCs [36–38] and the disklike QDs [25] modeled by an abrupt potential with an infinite barrier, it was shown that the mixing of the heavy- and light-hole states can significantly modify the energy spectrum and the wave function of the hole ground state, as well as its splitting. which can be caused by the anisotropy of the QD shape, the intrinsic crystal field, and an applied magnetic field [39]. Later, a full multiband $\boldsymbol{kp}$ model was developed for spherical NCs [40] and NC heterostructures with abrupt potential barriers [41], as well as for the pyramidal and disk-shaped epitaxial QDs [42–44]. Several models of parabolic potential with the valence-band degeneration taken into account were used for QDs of different shapes [35,45,53], not only within the effective mass approach but also as a modeling tool along with more elaborated atomistic calculations [46]. However, to the best of our knowledge, QDs with smooth but finite height potential confinement in all three spatial dimensions have been considered only within the single-band effective mass approximation so far. This simplified approximation can hardly be used for both epitaxial CdSe/ZnSe and colloidal CdSe/CdS QDs with a gradually varying composition [7,8,12].

In the present paper, we consider QDs with a shape that is close to either the spherical or the ellipsoidal one, and a smooth potential profile, which can be described by the Gaussians in all three spatial directions. We focus on the characteristics of a hole localized in such a potential taking into account the complex valence band structure in the framework of the Luttinger Hamiltonian. It is shown that the properties of the hole localized in potential with smooth profile, e.g., energy splittings caused by the shape anisotropy or an external magnetic field, might be very different from the properties of the hole localized in boxlike QDs with abrupt potential barriers.

The paper is organized as follows. In Sec. II, we introduce the regularities of our problem on the most intuitive example of a material with a single-band isotropic parabolic dispersion. In Sec. III, we move on to the characteristic properties of a hole localized in a spherically symmetric quantum dot with a top of the valence band that can be described by the Luttinger Hamiltonian. In Secs. IV and V, we consider the hole ground-state splitting due to the anisotropy of the QD potential, crystal field, and an external magnetic field. In the end, we summarize our results.

II. LOCALIZATION OF A PARTICLE IN QD WITH PARABOLIC OR GAUSSIAN PROFILE: SINGLE-BAND APPROXIMATION

To introduce the specifics of the carrier localization in the quantum dots described by the smoothly varying spatial potential $V(\boldsymbol{r})$ (r is the radial coordinate), we consider the Schrödinger equation $[\hat{H} + V(\boldsymbol{r})]\Psi = E\Psi$ with the single-band isotropic effective mass Hamiltonian

$$\hat{H} = \frac{\hbar^2 \hat{k}^2}{2m^*}. \tag{1}$$

Here, $\boldsymbol{k} = -i\nabla$ is the wave-vector operator and $m^* = m_{e(h)}$ is the electron (hole) effective mass. We consider the cases of the spherical symmetry $V(\boldsymbol{r}) = V(r)$ and axial symmetry $V(\boldsymbol{r}) = V(\rho,z)$ potentials, where $r^2 = x^2 + y^2 + z^2 = \rho^2 + z^2$ and x,y,z are are the Cartesian coordinates.

A. Spherically symmetric QD

We start with the spherical parabolic (harmonic oscillator) potential, which is the limiting case for the Gaussian potential

$$V_0(r) = \frac{\kappa}{2} r^2, \tag{2}$$

where κ is the spring constant. In the framework of the single-band effective mass approximation, the exact solutions of the problem with such a potential are well known. The spherical oscillator wave functions can be easily found as

$$\begin{aligned} \Psi_{nlm}(\mathbf{r}) &= R_{nl}(r) Y_{lm}(\Theta), \\ R_{nl}(r) &= \frac{1}{L^{3/2+l}} \left[\frac{2n!}{\Gamma(n+l+3/2)} \right]^{1/2} r^l \\ &\quad \times \exp\left(-\frac{r^2}{2L^2} \right) L_n^{l+1/2}\left(\frac{r^2}{L^2} \right), \end{aligned} \tag{3}$$

and correspond to the equidistant eigenenergies

$$E_N = \hbar\omega(N + 3/2), \quad N = 2n + l = 0,1,2\ldots. \tag{4}$$

Here, $\omega = \sqrt{\kappa/m^*}$ and $L = \sqrt{\hbar/m^*\omega}$ are the characteristic oscillator frequency and oscillator length, respectively, n, l, and m are principal, orbital, and magnetic quantum numbers, respectively, Y_{lm} are the spherical angular harmonics [48], and $L_n^{l+1/2}$ are the generalized Laguerre polynomials [47]. The ground-state energy and radial wave function of the particle localized in $V_0(r)$ are characterized by $n = 0, l = 0$ and given by

$$E_0 = \frac{3}{2}\hbar\omega = \frac{3}{2}\frac{\hbar^2}{m^* L^2} \tag{5}$$

and

$$R_0(r) = \frac{2}{\pi^{1/4} L^{3/2}} \exp\left(-\frac{r^2}{2L^2} \right). \tag{6}$$

The parabolic potential describes the QD with a smooth profile, however, yet it does not permit us to consider the QDs with a finite potential barrier outside the dot. To do so, we consider a potential of the Gaussian form,

$$V_G(r) = V_{off}\left[1 - \exp\left(-\frac{r^2}{a^2} \right) \right], \tag{7}$$

where V_{off} is the energy step (band offset) between the QD center and the surrounding medium, determined as $r > 3a$, while a can be used as a rough estimation of the QD radius. Near the QD center, at $r \ll a$, the Gaussian potential can be approximated as parabolic $V_G(r) \approx V_0(r)$ with the spring constant $\kappa = 2V_{off}/a^2$. To simplify the comparison of the

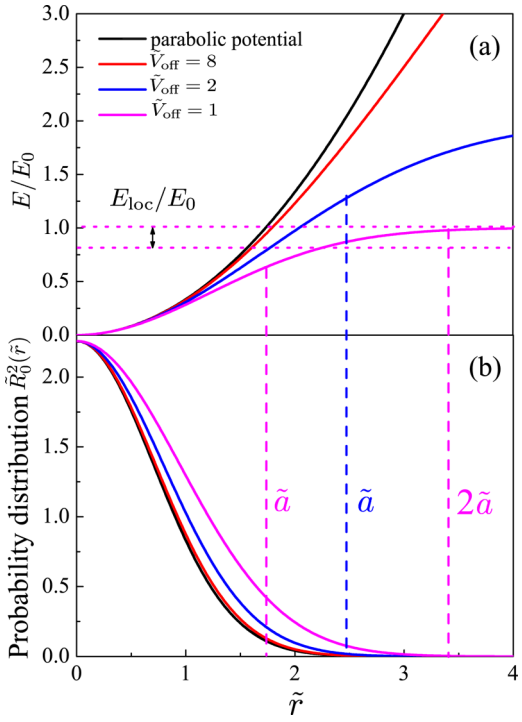

FIG. 1. (a) Dimensionless parabolic and Gaussian potentials with $\tilde{V}_{\rm off} = 8$, 2, and 1. (b) Probability distribution $\tilde{R}_0^2(\tilde{r})$ for different $\tilde{V}_{\rm off}$. Vertical dashed lines on (a) and (b) show the characteristic radii $\tilde{a}$ for $\tilde{V}_{\rm off} = 1$ and 2 and $2\tilde{a}$ for $\tilde{V}_{\rm off} = 1$. Horizontal dotted lines in (a) show the potential depth $\tilde{V}_{\rm off}$ and energy level E/E_0 for $\tilde{V}_{\rm off} = 1$.

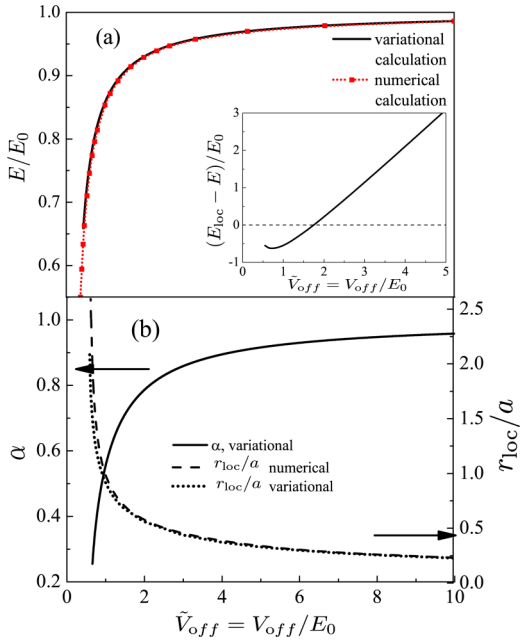

FIG. 2. (a) Dependence of the hole ground-state energy E/E_0 on the $\tilde{V}_{\rm off} = V_{\rm off}/E_0$, the inset shows the dimensionless difference between the localization energy and particle energy. (b) Dependencies of the variational parameter α and the localization radius $r_{\rm loc}/a$ on $\tilde{V}_{\rm off}$.

potentials characterized by the same spring constant k at the QD center and different potential barriers $V_{\rm off}$, we chose the parameters of the single-band parabolic problem – the ground-state energy E_0 and the oscillator length L – to be the energy and length units for all QDs. In these units, the parabolic and Gaussian potentials take the form

$$\tilde{V}_0(\tilde{r}) = V_0(r/L)/E_0 = \frac{1}{3}\tilde{r}^2, \tag{8}$$

$$\tilde{V}_{\rm G}(\tilde{r}) = V_{\rm G}(r/L)/E_0 = \tilde{V}_{\rm off}\left[1 - \exp\left(-\frac{\tilde{r}^2}{3\tilde{V}_{\rm off}}\right)\right], \tag{9}$$

where $\tilde{V}_{\rm off} = V_{\rm off}/E_0$ and $\tilde{r} = r/L$. Note that the spring constant is not included explicitly in Eqs. (8) and (9). It is, however, contained in expressions for our units L and E_0. This fact allows us to obtain the universal dependence of the localized particle wave function and energy spectrum on $\tilde{V}_{\rm off}$. The dimensionless parabolic and Gaussian potentials with different $\tilde{V}_{\rm off}$ are shown in Fig. 1(a), the chosen values of $\tilde{V}_{\rm off}$ correspond to characteristic radii $\tilde{a} = a/L = \sqrt{3\tilde{V}_{\rm off}} \approx 1.73$, 2.45, and 4.9. The vertical dashed lines show the characteristic radii $\tilde{a}$ for the shallowest dots with $\tilde{V}_{\rm off} = 1$ and 2; for $\tilde{V}_{\rm off} = 8$, the value of $\tilde{a}$ lies outside the scale of the figure, the parabolic potential has an infinite effective radius.

Since no exact solution exists for the particle in Gaussian potential, we found the wave function and energy of the ground state by two methods: numerical and variational. A numerical solution can be found by expanding the radial wave functions over the basis of the oscillator functions (3) and by diagonalizing the resulting matrix.

To obtain the ground-state energy by the variational procedure, we chose the dimensionless probe function $\tilde{R}_0(\tilde{r}) = R_0(r/L)L^{3/2}$ in the form

$$\tilde{R}_0 = \frac{2\alpha^{3/4}}{\pi^{1/4}} \exp\left(-\frac{\alpha\tilde{r}^2}{2}\right) \tag{10}$$

with α being the only trial parameter. With the probe function (10), we have the following expression for the particle ground-state energy as a function of α:

$$E(\alpha)/E_0 = \frac{\alpha}{2} + \tilde{V}_{\rm off} - \frac{3\sqrt{3}\alpha^{3/2}\tilde{V}_{\rm off}^{5/2}}{(1 + 3\alpha\tilde{V}_{\rm off})^{3/2}}. \tag{11}$$

Figure 1(b) shows the dimensionless probability distribution $\tilde{R}_0^2(\tilde{r})$ for the Gaussian QDs with different $\tilde{V}_{\rm off}$ and for parabolic QDs. Figure 2(a) shows the dependencies of the dimensionless ground-state energy E/E_0 on the $\tilde{V}_{\rm off} = V_{\rm off}/E_0$ and Fig. 2(b) shows the dependence of the minimizing value of the trial parameter α on $\tilde{V}_{\rm off}$. Panels (a) of Figs. 1 and 2 demonstrate that with the increase of $\tilde{V}_{\rm off}$ the ground-state energy and the wave function in the Gaussian potential approach those of the harmonic oscillator. While with a decrease of $\tilde{V}_{\rm off}$ the quantization energy E/E_0 decreases, the localization energy $E_{\rm loc}/E_0 = (V_{\rm off} - E)/E_0$ also decreases and becomes smaller than E for $\tilde{V}_{\rm off} < 2$ [see inset in Fig. 2(a)]. The bound state exists up to $\tilde{V}_{\rm off} \approx 0.55$ as it is shown by the numerical calculation; the variational calculation gives the bound state up to $\tilde{V}_{\rm off} \approx 0.65$.

The localization of the particle inside the QD can be characterized by the localization radius $\tilde{r}_{\rm loc} = r_{\rm loc}/L = \sqrt{\langle\tilde{r}^2\rangle} =$

$\sqrt{\int_0^\infty \tilde{R}_0^2 \tilde{r}^4 d\tilde{r}}$. We find $\tilde{r}_{\rm loc} \approx 1.23$ for the parabolic potential and $\tilde{V}_{\rm off} = 8$, and $\tilde{r}_{\rm loc} \approx 1.39$ and $\tilde{r}_{\rm loc} \approx 1.76$ for $\tilde{V}_{\rm off} = 2$ and 1, respectively. One can see that $\tilde{r}_{\rm loc} \approx 1.76$ only slightly exceeds the effective radius $\tilde{a} \approx 1.73$ for $\tilde{V}_{\rm off} = 1$ and $\tilde{r}_{\rm loc} < \tilde{a}$ for $\tilde{V}_{\rm off} = 2$ and higher potential barriers. In spite of the very small localization energy in the dots with $\tilde{V}_{\rm off} < 2$, the probability density $|\tilde{R}_0(\tilde{r})|^2$ is well localized inside these dots up to $\tilde{V}_{\rm off} = 1$. The dependence of $r_{\rm loc}/a = \tilde{r}_{\rm loc}/\tilde{a}$ on $\tilde{V}_{\rm off}$ is also shown in Fig. 2(b). Note that the radius $2a$ corresponds to the point where the Gaussian potential saturates: $V_{\rm G}(2a) \approx V_{\rm off}$. For the probe function (10), $\tilde{r}_{\rm loc} = \sqrt{1.5/\alpha}$ and $r_{\rm loc}/a = \tilde{r}_{\rm loc}/\tilde{a} = \sqrt{1/(2\alpha \tilde{V}_{\rm off})}$.

B. Axially symmetric nonspherical QD

Now we consider ellipsoidal axially symmetric QDs, where a parabolic confinement potential can be written as

$$V_p^a(r,z,\mu) = \frac{\kappa_\rho}{2}\rho^2 + \frac{\kappa_z}{2}z^2 = V_0(r) + \Delta V_p^a(\rho,z,\mu), \quad (12)$$

$$\Delta V_p^a(\rho,z,\mu) = \kappa\mu\left(z^2 - \frac{1}{3}r^2\right). \quad (13)$$

Here, the average spring constant is $\kappa = (2\kappa_\rho + \kappa_z)/3$ and we introduce the QD anisotropy parameter as

$$\mu = \frac{3}{2}\frac{(\kappa_z/\kappa_\rho - 1)}{(\kappa_z/\kappa_\rho + 2)} = \frac{(\kappa_z - \kappa_\rho)}{2\kappa}. \quad (14)$$

One can see that $\mu > 0$ corresponds to the case $\kappa_z > \kappa_\rho$ and thus describes a stronger confinement along the z direction (oblate QD). In the opposite case of $\mu < 0$, the confinement is stronger in the xy plane (prolate QD). Note that Eq. (12) is exact. It follows from (14) that

$$\kappa_\rho = \kappa\left(1 - \frac{2}{3}\mu\right), \quad \kappa_z = \kappa\left(1 + \frac{4}{3}\mu\right) \quad (15)$$

and the condition that $k_{\rho,z} \geqslant 0$ leads to only μ in the range $-3/4 \leqslant \mu \leqslant 3/2$ having a physical sense.

The exact solutions for the axially symmetric harmonic potential (12) are also well known. We introduce parameters L_x, L_y, L_z as oscillator lengths along x, y, z axes correspondingly, and note that in the axially symmetric potential $L_x = L_y = L$. In this case, the wave functions can be calculated from the Schrödinger equation for an axially symmetric harmonic oscillator:

$$\Psi_{n_x,n_y,n_z}(x,y,z) = \frac{1}{\sqrt{2^{n_x+n_y+n_z} n_x! n_y! n_z!}} \frac{\pi^{-3/4}}{L\sqrt{L_z}} \times H_{n_x}\left[\frac{x}{L}\right] H_{n_y}\left[\frac{y}{L}\right] H_{n_z}\left[\frac{z}{L_z}\right] \times \exp\left(-\frac{x^2+y^2}{2L^2} - \frac{z^2}{2L_z^2}\right), \quad (16)$$

and correspond to the equidistant eigenenergies

$$E_{n_x,n_y,n_z} = \hbar\omega(n_x + n_y + 2) + \hbar\omega_z(n_z + 1), \quad n_x, n_y, n_z = 0,1,2,\ldots. \quad (17)$$

Here, $H_n[x]$ are Hermite polynomials [47], $\omega = \sqrt{k_\rho/m}$, $\omega_z = \sqrt{k_z/m}$, and $L = \sqrt{\hbar/m\omega}, L_z = \sqrt{\hbar/m\omega_z}$. For the ground-state energy, we obtain

$$E_0^a = \frac{1}{2}\left(\frac{2\hbar^2}{mL^2} + \frac{\hbar^2}{mL_z^2}\right) = \frac{2E_0}{3}\left(\sqrt{1 - 2\mu/3} + \frac{1}{2}\sqrt{1 + 4\mu/3}\right) \approx E_0\left(1 - \frac{\mu^2}{9}\right). \quad (18)$$

One can see that (18) contains no linear μ correction to the ground-state energy. The same result can be readily observed by treating $\Delta V_p^a(\rho,z,\mu)$ as a perturbation.

We consider the anisotropic Gaussian potential with axial symmetry in the form

$$V_G^a(r,z,\mu) = V_{\rm off}\left[1 - \exp\left(-\frac{x^2+y^2}{a_x^2} - \frac{z^2}{a_z^2}\right)\right]. \quad (19)$$

The ground-state energy of the particle in such a potential can be found numerically by expanding the wave functions over the basis of the oscillator functions (16), diagonalizing the resulting matrix. The anisotropy can also be considered in the framework of the perturbation theory by two ways. One way is to find the isotropic and anisotropic parts of the Hamiltonian (19) as it was done in (12):

$$V_G^a(r,z,\mu) = V_{\rm off}\left[1 - \exp\left(-\frac{x^2+y^2}{a_x^2} - \frac{z^2}{a_z^2}\right)\right] \approx V_G(r) + \Delta V_p^a(r,z,\mu), \quad (20)$$

$$\Delta V_G^a(r,z,\mu) = \exp\left(-\frac{r^2}{a^2}\right)\Delta V_p^a(r,z,\mu),$$

where $a = \sqrt{3}a_x a_z/\sqrt{a_x^2 + 2a_z^2}$. The effective spring constants are introduced by analogy with the spherical QD: $\kappa_\rho = 2V_{\rm off}/a_x^2$ and $\kappa_z = 2V_{\rm off}/a_z^2$. The anisotropy parameter μ is defined in the same way as for the parabolic potential (14). The approximate expansion (20) keeps only terms linear on μ and is applicable for $\mu < 1$. Again, the first-order energy correction to the s symmetry ground state for the perturbation $\Delta V_G^a(r,z,\mu)$ vanishes. Using a numerical approach for $\mu < 1$, we found that the shift of the ground-state energy in the anisotropic Gaussian potential can be described as $E^a(\mu) \approx E^a(\mu = 0)[1 - \mu^2/9]$ by analogy with expression (18).

Alternatively, the anisotropy of the Gaussian potential can be treated by replacing the coordinates as $x \longrightarrow x(a_x/a)$, $y \longrightarrow y(a_x/a)$ and $z \longrightarrow z(a_z/a)$. The potential energy becomes isotropic in the new coordinates. However, the kinetic energy operator $\hat{H}$ acquires the additional term

$$\Delta\hat{H}_{\rm k}^{\rm a} = \frac{2\mu}{3}\frac{\hbar^2}{2m}\left(\hat{k}^2 - 3\hat{k}_z^2\right). \quad (21)$$

Again, the linear on μ energy correction to the ground state from $\Delta\hat{H}^{\rm a}$ vanishes.

III. SPHERICAL SYMMETRY PROBLEM FOR THE Γ_8 VALENCE BAND

We consider now the hole in the fourfold degenerate Γ_8 valence subband for semiconductors with large spin-orbit

splitting. The Luttinger Hamiltonian for such semiconductors in the spherical approximation can be written [33,49] as

$$\hat{H}_{\rm L} = \frac{\hbar^2}{2m_0}\left[\left(\gamma_1 + \frac{5}{2}\gamma\right)\hat{k}^2 - 2\gamma(\hat{\boldsymbol{k}}\boldsymbol{j})^2\right]. \tag{22}$$

Here, m_0 is the free electron mass, $\boldsymbol{j}$ is the hole internal angular momentum operator for $j = 3/2$, γ_1 and $\gamma = (2\gamma_2 + 3\gamma_3)/5$ are Luttinger parameters related to the light and heavy hole effective masses as $m_{\rm lh,hh} = m_0/(\gamma_1 \pm 2\gamma)$.

The first energy level of holes in spherical QDs in a semiconductor with a degenerate Γ_8 valence band is the $1S_{3/2}$ state [36,38]. It has a total angular momentum $\boldsymbol{J} = \boldsymbol{j} + \boldsymbol{l}$ with $J = 3/2$ and is fourfold degenerate with respect to its projection on the z axis. The wave functions of this state can be written as [49,50]

$$\Psi_M = 2\sum_{l=0,2}(-1)^{M-3/2}(i)^l R_l(r) \times \sum_{m+\mu=M}\begin{pmatrix} l & 3/2 & 3/2 \\ m & \mu & -M\end{pmatrix} Y_{l,m}u_\mu, \tag{23}$$

where $\begin{pmatrix} i & k & l \\ m & n & p\end{pmatrix}$ are the Wigner $3j$ symbols, and u_μ ($\mu = \pm 1/2, \pm 3/2$) are the Bloch functions of the fourfold degenerate valence band Γ_8 that can be found in Ref. [55]. The radial wave functions R_0 and R_2 in Eq. (23) are normalized, $\int(R_0^2 + R_2^2)r^2dr = 1$, and satisfy the system of differential equations (6) from Ref. [49,53], where the QD potential $V(r)$ instead of the Coulomb one is taken. Below we find R_0 and R_2 by numerical and variational methods.

A. Numerical method

To calculate numerically the energy spectrum and the eigen wave functions of the hole in a parabolic or a Gaussian quantum dot, we follow the approach described in Refs. [51,52]. We diagonalize the hole Hamiltonian matrix [49] calculated on a nonorthogonal basis, consisting of Gaussian functions times the polynomials of the lowest power, which behave correctly at $r = 0$:

$$R_0 = \sum_{i=1}^{N_{\max}=80} A_i \exp(-\alpha_i\tilde{r}^2), \qquad R_2 = \sum_{i=1}^{N_{\max}=80} B_i\tilde{r}\exp(-\alpha_i\tilde{r}^2). \tag{24}$$

Here, A_i and B_i are coefficients that are to be found by the diagonalization of the Hamiltonian matrix, α_i are chosen in the form of a geometrical progression from 10^{-6} to 10^3. The convergence of the calculation was controlled by modifying the basis (24): changing α_i and $N_{\max}$. The calculation was believed to be converged if the basis modification did not change the result. A rather large $N_{\max}$, as compared with Ref. [51], is necessary to obtain reliable results in the case of $\beta \to 0$, where $\beta = m_{\rm lh}/m_{\rm hh}$ is light to heavy hole effective mass ratio. For the limiting case $\beta = 1$, all $B_i = 0$ with a good accuracy and the use of the basis (24) gives the same results as the use of the basis (3). For $\beta \to 0$, the numerically calculated hole radial functions satisfy the exact differential condition [49]

$$\frac{dR_0}{dr} + \frac{dR_2}{dr} + \frac{3}{r}R_2 = 0 \tag{25}$$

with a good accuracy.

B. Variational method

We chose the trial functions R_0 and R_2 for the arbitrary value of β allowing them to satisfy the hole Hamiltonian [49] in two limits $\beta = 1$ and $\beta = 0$. If $\beta = 1$, the limiting case of the simple band dispersion is realized, and for the ground state, the probe radial functions should be chosen as $R_2 = 0$ and R_0 as given by (10). The exact solution for $\beta = 0$ is not known, however, the functions R_0 and R_2 must satisfy (25). Using these conditions and comparing the resulting functions with the numerically found solutions, we arrived at

$$R_2(r) = \frac{C}{L^{3/2}}\frac{\alpha\tilde{r}^2}{2}\left[\exp\left(-\frac{\alpha\tilde{r}^2}{2}\right) - \alpha_2\exp\left(-\frac{\alpha\beta^{0.3}\tilde{r}^2}{2}\right)\right],$$
$$R_0(r) = \frac{C}{L^{3/2}}\frac{3}{2}\left[\exp\left(-\frac{\alpha\tilde{r}^2}{2}\right) + \alpha_0\exp\left(-\frac{\alpha\beta^{0.3}\tilde{r}^2}{2}\right)\right] - R_2(r), \tag{26}$$

where α, α_0, and α_2 are the trial parameters and C is the normalization constant. The oscillator length L is defined as for the single band with heavy hole effective mass $m_{\rm hh}$ and $\tilde{r} = r/L$. Note that taking $\alpha_0 = \beta^{3/2}$ and $\alpha_2 = \beta^2$ and using $\beta^{0.5}$ instead of $\beta^{0.3}$ in the second exponent in R_0 and R_2, we arrive at the trial function used in Ref. [53] for the parabolic confinement potential.

C. Results: ground-state energy and radial wave functions

The ground-state energy $E_{1S_{3/2}}(\beta)$ is expressed in units of E_0 (with $m^* = m_{\rm hh}$) as follows:

$$E_{1S_{3/2}}(\beta) = \frac{3}{2}\frac{\hbar^2}{m_h L^2}\epsilon_{3/2}(\beta) = E_0\epsilon_{3/2}(\beta). \tag{27}$$

The dimensionless function $\epsilon_{3/2}(\beta)$ calculated variationally and numerically is shown in Fig. 3(a) for the parabolic potential and for the Gaussian potential with $\tilde{V}_{\rm off} = 8; 2; 1$. Figure 3(b) shows $\epsilon_{3/2}$ as a function of $\tilde{V}_{\rm off}$ for $\beta = 0.1$, 0.3, 0.7, and 1. There is a good matching between the two methods demonstrating the high accuracy of the variational method, which slightly decreases only for a very shallow dot potential (small $\tilde{V}_{\rm off}$ or very small β). This fact allows us to validate our choice of the trial function in the form (26). The critical value of $\tilde{V}_{\rm off}$ defining the appearance of the hole bound state increases with the decrease of β. Figures 4(a) and 4(b) show the dependencies of the ratio $r_{\rm loc}/a$ on $\tilde{V}_{\rm off}$ and β, where the localization radius $r_{\rm loc}$ is defined as $r_{\rm loc} = \sqrt{\langle r^2\rangle} = \sqrt{\int_0^\infty (R_0^2 + R_2^2)r^4dr}$. Figure 5 shows the dependencies of the variational parameters α, $\alpha_0(1-\beta)$, and α_2 on β for $\tilde{V}_{\rm off} = 8$, 2, and 1.

IV. ANISOTROPIC SPLITTING OF THE HOLE GROUND STATE

In this section, we consider the hole states in ellipsoidal QDs with $V(\boldsymbol{r})$ given by Eqs. (12) and (19). Additionally,

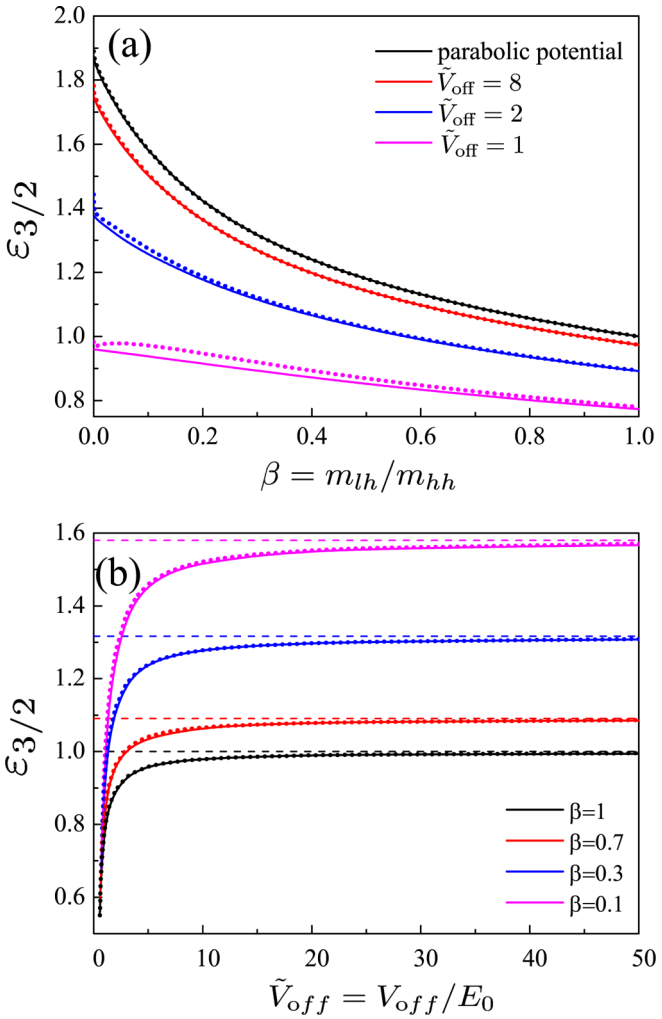

FIG. 3. Dimensionless ground-state energy $\varepsilon_{3/2}$ of the hole as a function of β for a parabolic potential and a Gaussian potential with $\tilde{V}_{\rm off} = 8; 2; 1$ (a) and as a function of $\tilde{V}_{\rm off}$ for $\beta = 0.1, 0.3, 0.7$, and 1 (b). Solid lines correspond to the numerical calculation, dotted lines, to the variational calculation. Dashed lines in (b) indicate the energy in the limit of the harmonic oscillator for the respective values of β.

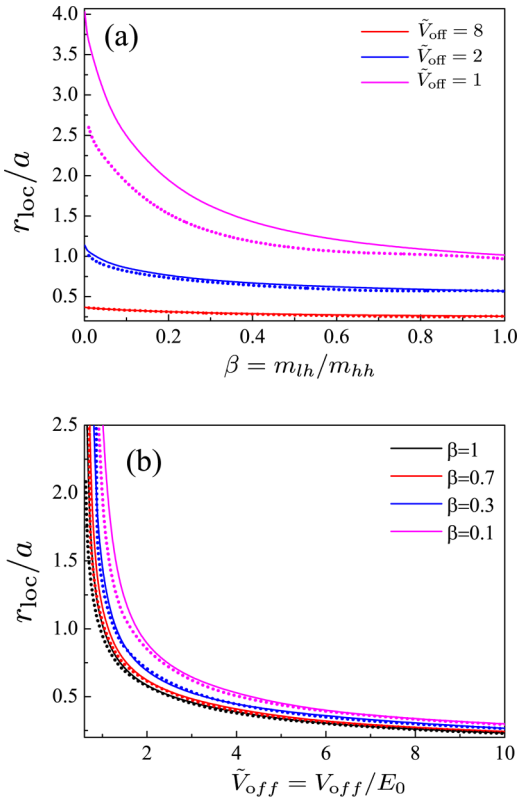

FIG. 4. Ratio of the localization radii and the characteristic dot radii, $r_{\rm loc}/a$, the function of β for the parabolic potential and the Gaussian potential with $\tilde{V}_{\rm off} = 8$, 2, and 1 (a) and as the function of $\tilde{V}_{\rm off}$ for $\beta = 0.1$, 0.3, 0.7, and 1 (b). Solid lines correspond to the numerical calculation and dotted lines to the variational calculation.

we consider the effect of the internal crystal field in wurtzite semiconductors, for example, CdSe, in the framework of the quasicubic approximation. The respective addition to the Hamiltonian is described by $\hat{V}^{\rm cr} = \Delta_{\rm cr}(5/8 - j_z^2/2)$, where $\Delta_{\rm cr}$ is the energy splitting of the light- and heavy-hole valence-band edge states in the bulk semiconductor [56].

The internal crystal field in wurtzite semiconductors and the axial anisotropy of the confinement potential lifts the degeneracy of the $1S_{3/2}$ hole ground-state in the quantum dot. The fourfold degenerate hole state is split into two doublets with $|M| = 3/2$ and $1/2$:

$$E_{1S_{3/2},M} = E^a_{1S_{3/2}} + \frac{\Delta}{2}\left(\frac{5}{4} - M^2\right), \tag{28}$$

where $\Delta = \Delta_{\rm int} + \Delta E^{\rm a}$, $\Delta_{\rm int}$ describes the effect of the internal crystal field, $\Delta E^{\rm a} = E_{1S_{3/2},1/2} - E_{1S_{3/2},3/2}$ and $E^a_{1S_{3/2}} = (E_{1S_{3/2},1/2} + E_{1S_{3/2},3/2})/2$ describe the hole ground-state splitting and the energy shift induced by the QD anisotropy, respectively. We calculate $\Delta_{\rm int}$, $\Delta E^{\rm a}$, and $E^a_{1S_{3/2}}$ numerically (see method description below) and determine the range of parameters where the effect of the crystal field and QD shape anisotropy can be considered as a perturbation. For these parameters, the splittings are calculated by the perturbation theory combined with the variationally found radial wave functions R_0 and R_2 of the spherical approximation.

A. Numerical method

To describe the hole states in nonspherical QDs, in general, one has to use the Hamiltonian $\hat{H}_{\rm L} + V(\boldsymbol{r})$ with allowance for $V(\boldsymbol{r})$ to be fully asymmetric. In order to calculate the hole energy spectrum and eigenfunctions, we diagonalize the Hamiltonian matrix, calculated on the orthonormal basis of anisotropic harmonic oscillator eigenfunctions:

$$\Psi_{n_x,n_y,n_z}(x,y,z) = \psi_{n_x}(x)\psi_{n_y}(y)\psi_{n_z}(z), \quad n_x,n_y,n_z = 1,\ldots,N, \tag{29}$$

where

$$\psi_{n_t}(t) = \frac{1}{\sqrt{2^{n_t} n_t!}}\left(\frac{1}{\pi \tilde{l}_t^2}\right)^{1/4} \exp\left(-\frac{t^2}{2\tilde{l}_t^2}\right) H_{n_t}\left(\frac{t}{\tilde{l}_t}\right), \quad t = x,y,z \tag{30}$$

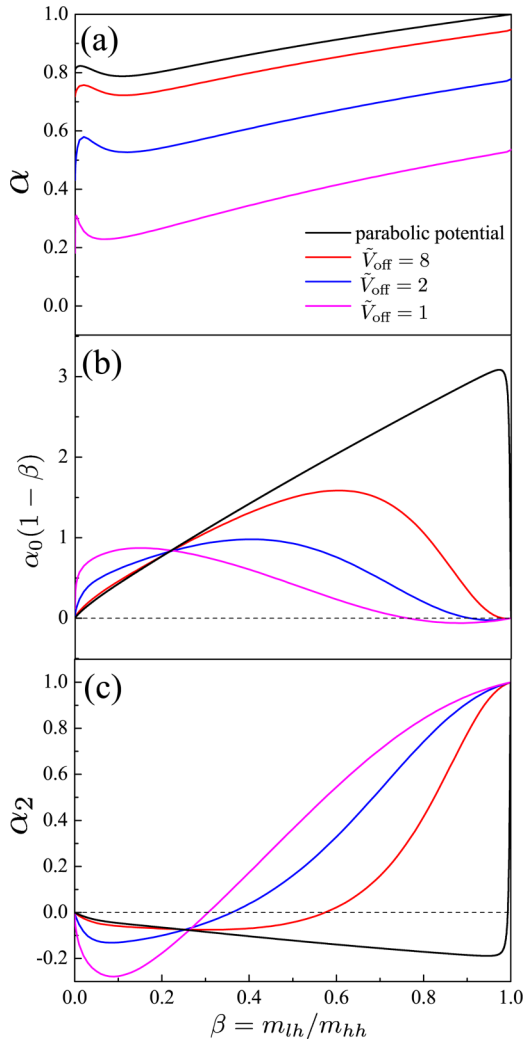

FIG. 5. Dependencies of the variational parameters α (a), $\alpha_0(1-\beta)$ (b), and α_2 (c) on β for parabolic potential and $\tilde{V}_{\rm off} = 8$, 2, and 1 and dependencies of the variational parameter α on $\tilde{V}_{\rm off}$ for $\beta = 0.1$, 0.3, 0.7, and 1 (d).

are the eigenfunctions of the harmonic oscillator with oscillator lengths $\tilde{l}_x = [\hbar^2(\gamma_1+\gamma)/m_0\kappa_x]^{1/4}$,$\tilde{l}_y = [\hbar^2(\gamma_1+\gamma)/m_0\kappa_y]^{1/4}$,$\tilde{l}_z = [\hbar^2(\gamma_1-2\gamma)/m_0\kappa_z]^{1/4}$. Such a basis corresponds to hole eigenfunctions, formed by Bloch states with momentum projection $j_z = \pm 3/2$ on the direction of the anisotropy axis. In order to check the convergence of the calculation, the second basis, corresponding to the holes formed by the Bloch states with a momentum projection $j_z = \pm 1/2$, is used. Note that even in the isotropic case, where $\kappa_x = \kappa_y = \kappa_z$, $\tilde{l}_{x,y} \neq \tilde{l}_z$ due to the difference of hole effective masses along the coordinate axes. The possible asymmetry of this basis may make it possible to account better for the QD potential geometry and increase the convergence rate of the calculation.

B. Results: comparison of numerical and perturbational calculations

1. Effect of the internal crystal field

The dependencies of the hole ground-state splitting $\Delta_{\rm int}$ on $\Delta_{\rm cr}$, calculated numerically for the holes confined in parabolic and Gaussian potentials are shown on Fig. 6(a) for $\beta = 0.15$. It is clear that for small values of $\Delta_{\rm cr}$ the corresponding curves can be linearized, and the effect of the crystal field can be considered as a perturbation [39,57]:

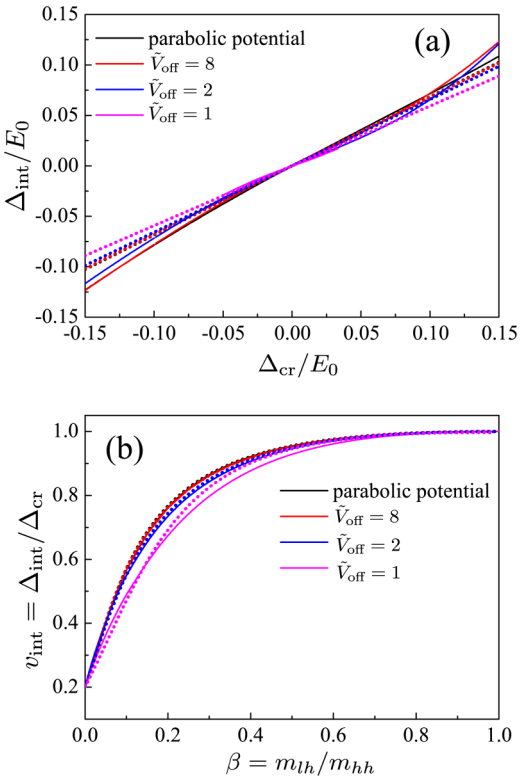

FIG. 6. (a) The hole ground-state splitting, calculated for $\beta = 0.15$, as a function of parameter $\Delta_{\rm cr}/E_0$ for parabolic and Gaussian potentials with $\tilde{V}_{\rm off} = 8$, 2, and 1. (b) The dimensionless function $v_{\rm int}(\beta)$ as a function of the light-hole to heavy-hole effective mass ratio β. Solid lines: results of numerical calculations, dotted lines: perturbation theory with the use of the trial functions.

$$\Delta_{\rm int} = \Delta_{\rm cr} v_{\rm int} = \Delta_{\rm cr} \int dr r^2 \left[R_0^2(r) - (3/5)R_2^2(r)\right]. \quad (31)$$

The function $v_{\rm int}$ depends on the ratio β and, generally, may depend on the form of the QD potential. The dependencies of $v_{\rm int}(\beta)$ for the parabolic and Gaussian potentials with $\tilde{V}_{\rm off} = 8$, 2, and 1 calculated numerically and obtained by using Eq. (31) with the trial function R_0 and R_2 in the form (26) are shown in Fig. 6(b). A good agreement between the two methods can be seen. The function $v_{\rm int}(\beta)$ only slightly depends on the value of $\tilde{V}_{\rm off}$, but the $|M| = 3/2$ states always correspond to the ground hole state [39,57]. The function $v_{\rm int}$ increases from 0.2 for $\beta = 0$ to 1 for $\beta = 1$. The value of $v_{\rm int}$ at $\beta = 0$ is determined by Eq. (25) resulting in $\int R_2^2 r^2 dr = \int R_0^2 r^2 dr = 1/2$. For $\beta = 1$, $v_{\rm int} = 1$ is explained by the vanishing of R_2.

2. Effect of the shape anisotropy

Figure 7(a) shows the dependencies of the anisotropy induced hole ground-state splitting $\Delta E^{\rm a}$ calculated numerically for parabolic and Gaussian potentials on the anisotropy parameter μ. This figure shows that in a rather wide range of

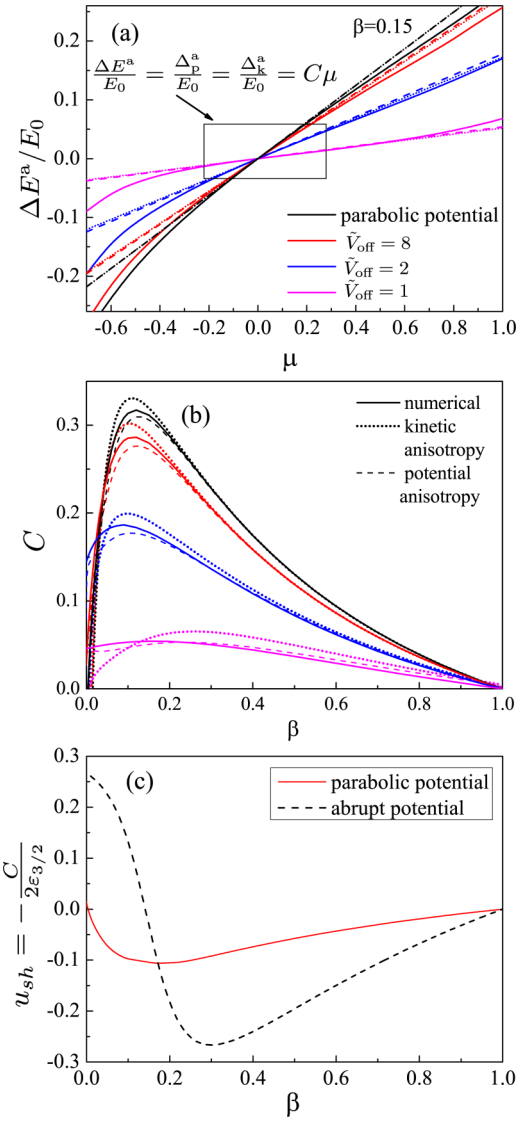

FIG. 7. (a) The dimensionless splitting of the hole ground state, calculated numerically, $\Delta E^a/E_0$ (solid lines), and by two perturbation theory methods: Δ^a_p/E_0 (dotted lines) and Δ^a_k/E_0 (dashed lines), calculated with numerically obtained functions $R_0(r)$ and $R_2(r)$ for parabolic and Gaussian QDs. (b) The coefficient of the linearization, $C = \Delta E^a/(E_0\mu)$, calculated numerically (solid curves) and using the trial functions via a perturbation in kinetic (dotted curves) and potential (dashed curves) energies. (c) The relative energy splitting, $u_{sh} = -\Delta E^a/(2\mu E_{3/2} = -C/2\varepsilon_{3/2}$, calculated for the parabolic (solid curve) and abrupt infinite potential (dashed curve).

μ these dependencies can be approximated as linear with a good accuracy. In this case, the splitting can be also found by the perturbation theory in two ways. One way is to consider as a perturbation the correction to the potential energy, V_p, introduced in Eq. (12) for parabolic potentials and in Eq. (20) for the Gaussian potentials. For such a perturbation, the hole energy splitting $\Delta E^a = \Delta^a_p$ can be found as [53]

$$\Delta^a_p = \frac{4\mu}{15}\frac{\hbar^2}{m_h L^4}\int dr r^4 R_0(r) R_2(r) \tag{32}$$

In the second way, one can use the change of coordinates (21) in order to obtain the perturbation correction to the hole kinetic energy [58,59]:

$$\hat{H}^a_k = \frac{2\mu}{3}\frac{\hbar^2}{2m_0}\left(\left(\gamma_1 + \frac{5}{2}\gamma\right)(\hat{k}^2 - 3\hat{k}_z^2) - 2\gamma\{(\hat{\boldsymbol{k}}\boldsymbol{j})^2 - 3[(\hat{\boldsymbol{k}}\boldsymbol{j})\hat{k}_z j_z]\}\right), \tag{33}$$

where $\{ab\} = (ab + ba)/2$. Then the hole energy splitting $\Delta E^a = \Delta^a_k$ can be found as [58]

$$\Delta^a_k = \frac{\mu\hbar^2}{3m_h}\left[I^a_1 - \frac{1}{5}I^a_2 + \frac{4}{5}I^a_3 - \frac{1}{\beta}\left(I^a_1 - \frac{1}{5}I^a_2 - \frac{4}{5}I^a_3\right)\right], \tag{34}$$

where

$$I^a_1 = \int r^2 dr\left[\frac{dR_0(r)}{dr}\right]^2,$$

$$I^a_2 = \int r^2 dr\left\{\left[\frac{dR_2(r)}{dr}\right]^2 + \frac{6R_2(r)^2}{r^2}\right\},$$

$$I^a_3 = \int r^2 dr R_2(r)\left[\frac{d^2R_0(r)}{dr^2} - \frac{dR_0(r)}{rdr}\right].$$

Calculations using the radial wave functions R_0 and R_2 found by the numerical method result into $\Delta^a_p = \Delta^a_k = C\mu E_0$ with a good accuracy for small μ, as shown in Fig. 7(a), and for all values of light-to-heavy hole effective mass ratio β. Figure 7(b) shows the linear coefficients C as functions of β. Dotted curves are calculated numerically, solid and dashed curves correspond to $C = \Delta^a_k/\mu/E_0$ and $C = \Delta^a_p/\mu/E_0$ calculated with the wave functions found via the variational procedure. This figure shows that the accuracy of the variational method is rather good. Moreover, the kinetic energy and potential energy corrections found with the variational wave functions give estimations of the value of C from above and from below, respectively.

For small values of μ, linear corrections to the energy shift of the central level position vanish and $E^a_{1S_{3/2}} = (E_{1S_{3/2},1/2} + E_{1S_{3/2},3/2})/2 \approx E_{1S_{3/2}}$. Numerical calculations show that for a complex valence band the following approximation $E^a_{1S_{3/2}} \approx E_{1S_{3/2}}[1 - \xi\mu^2/9]$ is valid, with the factor ξ being different from unity by no more than 10%. The parameter ξ is a function of β and V_{off}. Figure 7(c) shows the relative to the quantum size energy splitting, $u_{sh} = -\frac{\Delta E^a}{2\mu E_{3/2}} = -\frac{C}{2\varepsilon_{3/2}}$, introduced in Refs. [39,58] (the sign "−" is because of the opposite definition of the sign of anisotropy parameter μ) and calculated for parabolic and abrupt potentials. One can see that there is a significant difference between the dependencies caused by the different shape of the QD potential. The shape anisotropy at the abrupt potential in general induces a much larger relative splitting than that at the smooth one. Moreover, u_{sh} changes sign for an abrupt potential at $\beta \approx 0.15$, while remains always of the same sign in a smooth potential.

V. HOLE EFFECTIVE *g* FACTOR

In this section, we consider the effect of an external magnetic field on the hole states localized in quantum dots with a shape close to spherical. For this purpose, we follow the

conventional approach [25,33–35,39,55,56,60,61] and explore the hole representation of the Luttinger Hamiltonian with the external magnetic field $\boldsymbol{B}$ included in the spherical approximation [61]. In a weak magnetic field, the top of the degenerated valence band is split according to the Zeeman term

$$\widehat{H}_Z = -2\mu_B \varkappa (\boldsymbol{jB}). \tag{35}$$

Here, μ_B is the Bohr magneton, $\varkappa$ is the Luttinger magnetic parameter, and the lowest valence hole state has projection $j_z = 3/2$ on the direction of the magnetic field for the semiconductors with $\varkappa > 0$.

The effect of a weak external magnetic field on the holes confined in a potential of spherical symmetry can be considered as a perturbation. The resulting Zeeman splitting of the localized hole states is given by [35,39,61,62]

$$\widehat{H}_{\text{eff}} = -\mu_B g_{\text{h}} (\boldsymbol{JB}). \tag{36}$$

Here, g_{h} is the hole effective g factor. For the hole ground state with $J = 3/2$, its value can be determined via the radial wave functions R_0 and R_2 as [61]

$$g_{\text{h}} = 2\varkappa + \frac{8}{5}\gamma I_1^{\text{g}} + \frac{4}{5}[\gamma_1 - 2(\gamma + \varkappa)] I_2^{\text{g}}, \tag{37}$$

where

$$I_1^{\text{g}} = \int_0^\infty r^3 R_2(r) \frac{dR_0(r)}{dr} dr, I_2^{\text{g}} = \int_0^\infty r^2 R_2^2(r) dr. \tag{38}$$

The integrals I_1^{g} and I_2^{g} describe the effect of the light- and heavy-hole mixing induced by the confining potential. Their values depend on the light-to-heavy hole effective mass ratio β and do not depend on the QD size [39,62]. In the limit $\beta = 1$, the hole mixing vanishes and $g_{\text{h}}(\beta = 1) = 2\varkappa$. In the opposite case, $\beta \to 0$, the values of the mixing integrals can be found analytically as $I_1^{\text{g}} = -3/4$ and $I_2^{\text{g}} = 1/2$ in any spherical symmetry potential using the differential condition (25). This results in [61]

$$g_{\text{h}}(\beta = 0) = \frac{6}{5}\varkappa + \frac{2}{5}\gamma_1 - 2\gamma. \tag{39}$$

Using the relation $\varkappa = -2/3 + 5\gamma/3 - \gamma_1/3$ [62,63], we obtain from Eq. (39) that $g_{\text{h}}(\beta = 0) \approx -0.8$ corresponding to the lowest hole state with projection $M = -3/2$ on the magnetic field. Thus, in semiconductors with small values of β, the mixing of the valence subbands may result in different ordering of the Zeeman sublevels comparing with the free valence-band edge states.

We examine further the effect of the valence-band mixing on the hole effective g factor in the QDs with different potential profiles. The dependencies of the mixing integrals I_1^{g} and I_2^{g} on β, calculated variationally (dotted lines) and numerically (solid lines) for the parabolic (black lines) and Gaussian, with $\tilde{V}_{\text{off}} = 1$, smooth potentials and the infinite abrupt potential, respectively, are shown on Fig. 8. In fact, the difference between the values calculated variationally and numerically for smooth potentials is very small for any mass ratio and

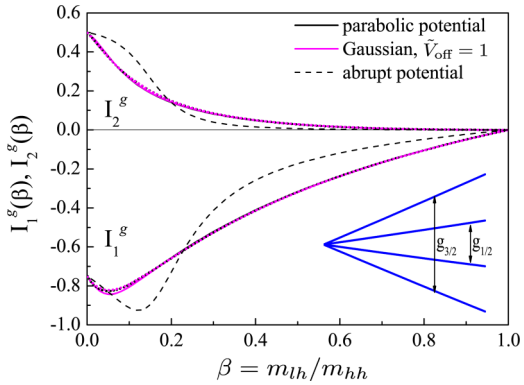

FIG. 8. Dimensionless integrals I_1^{g} and I_2^{g}, defining the hole ground-state g factor in a spherical quantum dot, Eq. (37), with parabolic, Gaussian with $\tilde{V}_{\text{off}} = 1$, and abrupt infinite potentials [39] as a function of β. Solid lines correspond to the variational calculation, dotted lines to the numerical calculation, dashed lines correspond to the abrupt infinite potential.

can be hardly seen in this figure; this is also true for the difference between the values calculated for the parabolic and Gaussian smooth potentials. This demonstrates the exceptional accuracy of the variational method. Moreover, I_1^{g} and I_2^{g} are practically independent of $\tilde{V}_{\text{off}}$ (as long as a confined level in a Gaussian QD exists), while the hole wave functions are strongly dependent on $\tilde{V}_{\text{off}}$ (see, for example, Fig. 5 showing the resulting trial parameters). As a result, the g factor for the hole in the parabolic and Gaussian QDs can be estimated with a good accuracy using a simple universal approximation of the β dependence for mixing integrals:

$$\begin{aligned} I_1^{\text{g}} &\approx e^{-5.145\beta}(1-\beta) \\ &\quad \times (-29.77\beta^5 - 37.97\beta^3 + 7.15\beta^2 - 7.77\beta - 0.75), \\ I_2^{\text{g}} &\approx 0.5 e^{-7.35\beta^{1.127}}(1-\beta)(14.23\beta^{2.58} + 1). \end{aligned} \tag{40}$$

In contrast, Fig. 8 shows a noticeable difference between mixing integrals I_1^{g} and I_2^{g} calculated for smooth potentials and for an infinite abrupt potential, respectively [39]. It means that the magneto-optical properties of QDs with smooth and abrupt potentials can be quite different.

In the spherically symmetric QDs, the hole ground-state in zero magnetic field is fourfold degenerate with respect to the momentum projection M. Hence, in agreement with Eq. (36), in weak magnetic fields, the ground state splits into four equidistant sublevels (see the inset in Fig. 8). So, two effective g factors can be introduced in this case: $g_{1/2} = g_{\text{h}}$ for the splitting of the states with a momentum projection $M \pm 1/2$ on the magnetic field direction and $g_{3/2} = 3g_{\text{h}}$ for the states with a momentum projection $M = \pm 3/2$. The lowest hole state is always $M = -3/2$ for semiconductors with $\beta \to 0$ and $M = +3/2$ ($M = -3/2$) for semiconductors with $\varkappa > 0$ ($\varkappa < 0$) and $\beta \to 1$.

In the axially symmetric QD, the joint effect of the anisotropy and magnetic field depends on the direction of the magnetic field with respect to the direction of the anisotropy axis z. In the case of small anisotropy, for $\boldsymbol{B}||z$, the hole effective g factors for $M = \pm 3/2$ and $M = \pm 1/2$ states remains the same: $g_{3/2} = 3g_{\text{h}}$ and $g_{1/2} = g_{\text{h}}$, respectively [35].

For $\boldsymbol{B} \perp z$, they become strongly anisotropic: the linear on $\boldsymbol{B}$ splitting of $\pm 3/2$ states vanishes, whereas the splitting of $\pm 1/2$ states is described by an effective g factor equal to $g_{1/2}^{\perp} = 2g_{\mathrm{h}}$. Such a consideration is valid while the magnetic field induced splitting is smaller than the zero-field energy splitting ΔE^{a}. In addition, the $\boldsymbol{B} \perp z$ mixes the hole states with $M = \pm 3/2$ and $\pm 1/2$ [39,62].

In the case of highly anisotropic QDs, i.e., in the limit of the quantum disk or quantum wire, it can be convenient to describe the hole states in the framework of the Luttinger spinors introduced in Ref. [25] and classify the hole states by the parity quantum number and the z component of the total angular momentum, which determine their splitting in the magnetic field. In these cases, the hole g factors are substantially different from the values of $g_{3/2}$ and $g_{1/2}$, calculated above. The respective anisotropic g factor values were calculated in Ref. [35] for the model of the parabolic potential.

VI. DISCUSSION

In this paper, we presented a detailed study of the hole states in quantum dots with a smooth potential shape of rotational symmetry, which can be realized in II-VI structures. We developed a variational approach with only three trial parameters, which allowed us to calculate with a good accuracy not only the hole energy but also its g factor and energy splitting of ground state caused by the anisotropy of the quantum dot shape or the crystal field. These quantities proved to be strongly dependent on the wave function and, therefore, very sensitive to the choice of the trial function. For example, we have found that the simplified trial functions with the only trial parameter from Ref. [53] predict the hole ground-state energy with a good accuracy, however, they do not allow to calculate the hole g factor and anisotropy-induced splittings. The accuracy of the these trial functions and the developed variational method are verified by comparing the obtained results with numerical calculations. The advantage of the variational method is to allow one to have the hole envelope wave function in a simple analytical form that can be rather easily used for further modeling, e.g., of the multiexciton states in the QDs. At the same time, the developed numerical method allows one to calculate the whole energy spectrum including the excited states of the holes in a smooth Gaussian-like potential. To the best of our knowledge, neither a variational method nor numerical calculations (including the atomistic approaches) for the hole states in QDs with such a potential profile have been reported before.

The general dependencies of the hole ground-state characteristics (energy and localization radius) on the QD potential depth and light-to-heavy hole effective mass ratio are calculated for spherical QDs. The effect of the QD anisotropy (potential shape or internal crystal field) on the hole ground state is considered. General dependencies of the hole ground-state splitting on the potential depth and light-to-heavy hole effective mass ratio are obtained. In addition, the Zeeman splitting of the hole ground state due to the external magnetic field is studied. It is shown that the dependence of the hole effective g factor on the depth of the QD potential is negligible and its dependence on β for the QDs with an approximately spherical shape can be well approximated by universal analytical expressions. Moreover, the results obtained in Ref. [35] for the hole effective g factors in QDs modeled by ellipsoidal parabolic potential profiles of arbitrarily anisotropy can be used for the case of the Gaussian-shaped QDs as well. Thus, in the limit of weak magnetic fields, the effective hole g factor is determined solely by the potential profile type but does not depend on its size and barrier height. These results are in line with the known independence of the effective g factor of the localization energy of a hole bound to a deep or Coulomb-like acceptor center [61,64,65] and of the QD size [39,62]. In contrast, the Zeeman splittings and the zero field splittings caused by the QD shape anisotropy are quite different for the abrupt and the smooth confining potentials. Such a difference may include even a different ordering of the hole states both in zero and in an external magnetic field. Therefore the combination of the smooth and abrupt potentials, e.g., by variation of the QD composition, opens new possibilities for the design of structures with the needed properties of the hole states.

Let us discuss the applicability of the developed model to the II-VI QDs with a gradually varying concentration [7,8,12]. The potential profile in such dots, indeed, can be approximated by the Gaussian shape. However, a variation of the concentration implies also a spatial variation of the effective mass parameters. In II-VI QDs, the variation of the effective mass parameters is not large and for the first approximation the mean values can be used with our model. The energy corrections caused by the effective mass spatial variation are expected to be of the same order of magnitude as the corrections caused by the nonparabolicity of the energy dispersion (terms $\propto \hat{k}^4$) [66]. Therefore they should be considered in the framework of the Kane $\boldsymbol{k}\boldsymbol{p}$ model taking into account the interaction between the conduction and the valence bands, and that may be a subject of a future study.

ACKNOWLEDGMENTS

The authors are thankful to T. V. Shubina and R. A. Suris for stimulating discussions. The work was supported by Russian Science Foundation (Project No. 14-22-00107).

[1] S. V. Ivanov, S. V. Sorokin, and I. V. Sedova, Molecular beam epitaxy of wide-gap II-VI laser heterostructures, in *Molecular Beam Epitaxy* (Elsevier, Waltham, MA, 2013), pp. 611–630.

[2] S. V. Sorokin, S. V. Gronin, I. V. Sedova, M. V. Rakhlin, M. V. Baidakova, P. S. Kop'ev, A. G. Vainilovich, E. V. Lutsenko, G. P. Yablonskii, N. A. Gamov, E. V. Zhdanova, M. M. Zverev, S. S. Ruvimov, and S. V. Ivanov, Semiconductors **49**, 331 (2015).

[3] S. Strauf, S. M. Ulrich, K. Sebald, P. Michler, T. Passow, D. Hommel, G. Bacher, and A. Forchel, Phys. Status Solidi B **238**, 321 (2003).

[4] A. Tribu, G. Sallen, T. Aichele, R. André, J.-P. Poizat, C. Bougerol, S. Tatarenko, and K. Kheng, Nano Lett. **8**, 4326 (2008).

[5] O. Fedorych, C. Kruse, A. Ruban, D. Hommel, G. Bacher, and T. Kümmell, Appl. Phys. Lett. **100**, 061114 (2012).

[6] A. Klochikhin, A. Reznitsky, B. D. Don, H. Priller, H. Kalt, C. Klingshirn, S. Permogorov, and S. Ivanov, Phys. Rev. B **69**, 085308 (2004).

[7] N. Peranio, A. Rosenauer, D. Gerthsen, S. V. Sorokin, I. V. Sedova, and S. V. Ivanov, Phys. Rev. B **61**, 16015 (2000).

[8] D. Litvinov, M. Schowalter, A. Rosenauer, B. Daniel, J. Fallert, W. Löffler, H. Kalt, and M. Hetterich, Phys. Status Solidi A **205**, 2892 (2008).

[9] V. D. Kulakovskii, G. Bacher, R. Weigand, T. Kümmell, A. Forchel, E. Borovitskaya, K. Leonardi, and D. Hommel, Phys. Rev. Lett. **82**, 1780 (1999).

[10] M. Syperek, D. R. Yakovlev, I. A. Yugova, J. Misiewicz, I. V. Sedova, S. V. Sorokin, A. A. Toropov, S. V. Ivanov, and M. Bayer, Phys. Rev. B **84**, 085304 (2011).

[11] A. Reznitsky, M. Eremenko, I. V. Sedova, S. V. Sorokin, and S. V. Ivanov, Phys. Status Solidi B **252**, 1717 (2015).

[12] M. Nasilowski, P. Spinicelli, G. Patriarche, and B. Dubertret, Nano Lett. **15**, 3953 (2015).

[13] G. E. Cragg, and Al. L. Efros, Nano Lett. **10**, 313 (2010).

[14] F. Garcia-Santamaria, S. Brovelli, R. Viswanatha, J. A. Hollingsworth, H. Htoon, S. A. Crooker, and V. I. Klimov, Nano Lett. **11**, 687 (2011).

[15] W. K. Bae, L. A. Padilha, Y.-S. Park, H. McDaniel, I. Robel, J. M. Pietryga, and V. I. Klimov, ACS Nano **7**, 3411 (2003).

[16] J. I. Climente, J. L. Movilla, and J. Planelles, Small **8**, 754 (2012).

[17] M. Korkusinski, O. Voznyy, and P. Hawrylak, Phys. Rev. B **82**, 245304 (2010).

[18] M. Zielinski, Y. Don, and D. Gershoni, Phys. Rev. B **91**, 085403 (2015).

[19] R. Singh and G. Bester, Phys. Rev. Lett. **104**, 196803 (2010).

[20] Al. L. Efros and A. L. Efros, Sov. Phys. Semicond. **16**, 772 (1982).

[21] L. E. Brus, J. Chem. Phys. **80**, 4403 (1984).

[22] J. L. Marin, R. Rier, and S. A. Cruz, J. Phys. Condens. Matter **10**, 1349 (1998).

[23] G. Pellegrini, G. Mattei, and P. Mazzoldi, J. Appl. Phys. **97**, 073706 (2005).

[24] D. Schooss, A. Mews, A. Eychmuller, and H. Weller, Phys. Rev. B **49**, 17072 (1994).

[25] L. G. C. Rego, P. Hawrylak, J. A. Brum, and A. Wojs, Phys. Rev. B **55**, 15694 (1997).

[26] Xie Wen-Fang, Physica B **358**, 109 (2005).

[27] W. Que, Phys. Rev. B **45**, 11036 (1992).

[28] J. Adamowski, M. Sobkowicz, B. Szafran, and S. Bednarek, Phys. Rev. B **62**, 4234 (2000).

[29] M. Ciurla, J. Adamowski, B. Szafran, and S. Bednarek, Physica E **15**, 261 (2002).

[30] Xie Wen-Fang, Superlattices Microstruct. **46**, 693 (2009).

[31] B. Szafran, S. Bednarek, and J. Adamowski, Phys. Rev. B **64**, 125301 (2001).

[32] A. Wojs, P. Hawrylak, S. Fafard, and L. Jacak, Phys. Rev. B **54**, 5604 (1996).

[33] J. M. Luttinger, Phys. Rev. **102**, 1030 (1956).

[34] M. Kubisa, K. Ryczko, and J. Misiewicz, Phys. Rev. B **83**, 195324 (2011).

[35] M. A. Semina and R. A. Suris, Semiconductors **49**, 797 (2015).

[36] Al. L. Efros and A. V. Rodina, Solid State Commun. **72**, 645 (1989).

[37] J. B. Xia, Phys. Rev. B **40**, 8500 (1989).

[38] A. I. Ekimov, F. Hache, M. C. Schanne-Klein, D. Ricard, C. Flytzanis, I. A. Kudryavtsev, T. V. Yazeva, A. V. Rodina, and Al. L. Efros, J. Opt. Soc. Am. B **10**, 100 (1993).

[39] Al. L. Efros, M. Rosen, M. Kuno, M. Nirmal, D. J. Norris, and M. Bawendi, Phys. Rev. B **54**, 4843 (1996).

[40] Al. L. Efros and M. Rosen, Phys. Rev. B **58**, 7120 (1998).

[41] W. Jaskolski and G. W. Bryant, Phys. Rev. B **57**, R4237 (1998).

[42] C. Pryor, Phys. Rev. B **57**, 7190 (1998).

[43] O. Stier, M. Grundmann, and D. Bimberg, Phys. Rev. B **59**, 5688 (1999).

[44] M. Tadic, F. M. Peeters, and K. L. Janssens, Phys. Rev. B **65**, 165333 (2002).

[45] R. Rinaldi, P. V. Giugno, R. Cingolani, H. Lipsanen, M. Sopanen, J. Tulkki, and J. Ahopelto, Phys. Rev. Lett. **77**, 342 (1996).

[46] M. Korkusinski and P. Hawrylak, Phys. Rev. B **87**, 115310 (2013).

[47] M. Abramowitz and I. Stegun, *Handbook of Mathematical Functions with Formulas, Graphs, and Mathematical Tables* (Dover, New York, 1965).

[48] A. R. Edmonds, *Angular Momentum in Quantum Mechanics* (Princeton University Press, Princeton, NJ, 1957).

[49] B. L. Gel'mont and M. I. D'yakonov, Sov. Phys. Semicond. **5**, 905 (1971).

[50] Note that the factor $(i)^l$ introduced because we use the definition of spherical harmonics Y_{lm} as given in Ref. [48] while in Ref. [49], the spherical harmonics were defined according to Ref. [54].

[51] N. O. Lipari and A. Baldereschi, Phys. Rev. Lett. **25**, 1660 (1970).

[52] A. Baldereschi and N. O. Lipari, Phys. Rev. B **8**, 2697 (1973).

[53] A. V. Rodina and Al. L. Efros, Phys. Rev. B **82**, 125324 (2010).

[54] L. D. Landau and E. M. Lifshitz, *Quantum Theory*, 2nd ed. (Pergamon, Oxford, 1965).

[55] E. L. Ivchenko, *Optical Spectroscopy of Semiconductor Nanostructures* (Alpha Science International Ltd., Harrow, UK, 2005).

[56] G. L. Bir and G. E. Pikus, *Symmetry and Strain-Induced Effects in Semiconductors* (Wiley, New York, 1974).

[57] Al. L. Efros, Phys. Rev. B **46**, 7448 (1992).

[58] Al. L. Efros and A. V. Rodina, Phys. Rev. B **47**, 10005(R) (1993).

[59] There is the misprint in Ref. [58]: m_0 in Eq. (8) should be replaced by $2m_h$ [53].

[60] L. Roth, B. Lax, and S. Zwerdling, Phys. Rev. **114**, 90 (1959).

[61] B. L. Gel'mont and M. I. D'yakonov, Sov. Phys. Semicond. **7**, 1345 (1973).

[62] Al. L. Efros, in *Semiconductor and Metal Nanocrystals: Synthesis and Electronic and Optical Properties*, edited by V. I. Klimov (Marcel Dekker, New York, 2004).

[63] G. Dresselhaus, A. F. Kip, and C. Kittel, Phys. Rev. **98**, 368 (1955).

[64] A. V. Malyshev and I. A. Merkulov, Phys. Solid State **39**, 49 (1997) [Fiz. Tverd. Tela **39**, 58 (1997)].

[65] A. V. Malyshev, I. A. Merkulov, and A. V. Rodina, Phys. Status Solidi B **210**, 865 (1998).

[66] E. E. Takhtamirov and V. A. Volkov, JETP **89**, 1000 (1999).